# ADAPTING THE SIR ALGORITHM TO ASCAT

*Richard D. Lindsley and David G. Long*

Brigham Young University
MERS Laboratory
459 CB, Provo, UT 84602

## ABSTRACT

Scatterometers have been launched primarily to measure ocean winds. The value of scatterometer data is increased by application of the SIR (Scatterometer Image Reconstruction) algorithm. The SIR algorithm enhances the effective resolution of the scatterometer data to support its use for other studies. SIR has been used successfully on several scatterometers, including QuikSCAT. In this paper, we describe how the SIR algorithm is adapted to ASCAT data. Using SZF data from ASCAT leads to the best resolution enhancement. SIR requires an estimate of the spatial extent for each measurement. We detail our method to estimate an approximate spatial response function for each ASCAT measurement. Finally, SIR parameters are tuned for use with ASCAT.

***Index Terms—*** Remote sensing, Spatial resolution enhancement, Image reconstruction

## 1. INTRODUCTION

The ESA/EUMETSAT ASCAT (Advanced SCATterometer) is one of the latest remote sensing instruments in Earth orbit. ASCAT is a C-band scatterometer deployed on the MetOp-A platform. It operates at 5.255 GHz using vertically-polarized antennas [1]. Although it is designed to measure wind fields over the oceans, the radar backscatter over land and ice is collected, proving useful in land and ice studies.

The SIR (Scatterometer Image Reconstruction) algorithm [2, 3] increases the resolution of scatterometer data and has been successfully used for other scatterometers such as QuikSCAT, NSCAT, and ERS. SIR has not previously been applied to ASCAT.

The Brigham Young University (BYU) Microwave Earth Remove Sensing (MERS) lab has an extant time series of scatterometer data from AMI (advanced microwave instrument), a C-band scatterometer flown on two platforms (ERS-1 and ERS-2). The ERS data (1992–2001) has previously been processed with SIR as part of the Scatterometer Climate Record Pathfinder (`www.scp.byu.edu`). Processing ASCAT data with SIR extends this database of C-band scatterometer data.

SIR-processed ASCAT data also allows the comparison of C-band SIR data with contemporary Ku-band SIR data. Data from QuikSCAT, a Ku-band scatterometer, has been processed using SIR for the lifetime of the instrument (1999–2009). Adding C-band data from ASCAT complements the QuikSCAT data and is useful to compare the same geographic regions across the two bands. For example, polar icebergs are visible in both bands, but occasionally are easier to distinguish in one band or the other.

The SIR algorithm enhances the effective spatial resolution of the data, assuming sufficiently dense sampling. ASCAT samples are dense enough for the SIR algorithm due to the three look directions of the antenna beams: fore, mid, and aft. Combining the data from multiple passes provides a dense sampling.

SIR enhances the resolution of scatterometer data by combining data from overlapping measurements over the same region. Over a range of incidence angles $\theta_i$, measurements of radar backscatter $\sigma^0$ over land and ice can be modeled as

$$10 \log_{10} \sigma^0 = \mathcal{A} + (\theta_i - 40^\circ)\mathcal{B}, \tag{1}$$

in which $\mathcal{A}$ and $\mathcal{B}$ are functions of polarization, azimuth angle, and physical characteristics of the region corresponding to the $\sigma^0$ measurement. $\mathcal{A}$ is in dB and represents the $\sigma^0$ value normalized to a 40° incidence angle. $\mathcal{B}$ is in dB/° and is a measure of the dependence of $\sigma^0$ on $\theta_i$ [2, 3, 4, 5].

This paper details how we adapt the SIR algorithm to work with ASCAT. We consider using both SZR and SZF ASCAT data. The spatial response function used in either case is discussed. We optimize the tuning parameters of the SIR algorithm using various metrics and provide sample images of the final SIR output.

## 2. USING SIR ON ASCAT DATA

ASCAT data as processed by EUMETSAT come in three product types: SZO, SZR, and SZF. The SZO and SZR products contain spatially averaged $\sigma^0$ measurements. SZO data is not considered in this paper. SZR data is spatially averaged on a 12.5 km grid. SZF data contains the $\sigma^0$ values before spatial averaging.

Because of the similarity of ASCAT to previous scatterometers, much of the effort in applying the SIR algorithm to ASCAT SZR data has been previously done with the ERS scatterometer. ERS uses a spatial response function with a ∼50 km resolution for each $\sigma^0$ measurement. We use the same response function, but scale it by half to fit the ∼25 km resolution used by ASCAT SZR data. Finally, the extant ERS code was adapted to create a working ASCAT SZR SIR implementation. Example SIR images are considered below.

Applying the SIR algorithm to the SZF data requires some more attention. We present some background to the data format and illustrate our method to approximate the $\sigma^0$ spatial response.

### 2.1. Background

The ASCAT SZF files are organized such that each measurement and its associated data are grouped into a ‘node.’ Each of the six antenna beams are partitioned into 256 nodes. Each node contains several values: (1) the node center, reported in latitude and longitude, (2) the normalized radar cross-section, or $\sigma^0$, measurement for the node, and (3) the incidence angle $\theta_i$ for that node.

A critical input to the SIR algorithm is a knowledge of the spatial response function of each $\sigma^0$ measurement. Unfortunately, detailed

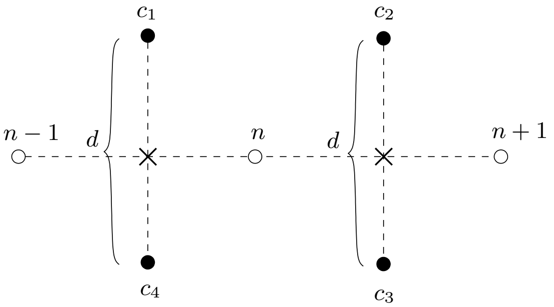

**Fig. 1**. Determining slice corners $c_1, \ldots, c_4$. The empty circles are node positions for three consecutive nodes. Node midpoints are marked with an X. Slice corners are indicated by the filled black circles. The width of a slice is determined by the distance between node midpoints, and the length of a slice is determined by $d$, as explained in the text.

information on individual ASCAT $\sigma^0$ measurement spatial response functions is limited. Ideally, a full 3D response function for each SZF node would be used. Instead, we use a binary approximation of the main lobe, where the approximate response is set to 1 from the response center to where the two-way response drops off 6 dB, and 0 elsewhere (this ignores any contributions of the side lobes to $\sigma^0$). This approximation traces out a two-dimensional ellipsoidal-like binary mask and is roughly equivalent to the spatial extent of a node. A similar approach is used for 'slice' measurements from QuikSCAT [6].

Without knowing the precise shape of the ellipsoidal mask, we approximate it by determining a rectangular area that is equivalent to the true spatial extent. We term the rectangular area for each node a 'slice,' echoing the terminology used for QuikSCAT. Because of onboard range filtering, the effective response functions of neighboring nodes may overlap. To simplify computation, we do not fully account for single-pulse slice overlap in this spatial response approximation. Because the slice is rectangular, the area bounded by each slice is characterized by the location of the four corners of the slice.

### 2.2. Method

Each node $n$ (except the first and last nodes in a beam) is bordered on either side by another node. To find the slice boundaries for a node $n$, the slice width is determined by using the midpoint between a node and its two adjacent nodes. This is indicated in Fig. 1 by the two X marks. The slice length $d$ is determined by using the 3-dB azimuthal beamwidth of the antenna ($\theta$) and the slant range $\rho_d$ to node $n$ in the relation $d = \rho_d \cdot \theta$, making use of the small-angle approximation. The two-way 6-dB beamwidths for the middle two beams and for the outer four beams were provided to us.

Figure 1 shows how the slice length, $d$, is used to find the four slice corners after the midpoints are found. For simplicity, we approximate the sides of the slices to be perpendicular to the along-beam direction. The slant range $\rho_d$ is not provided in the SZF file but must be approximated by assuming a mean altitude for ASCAT. $\rho_d$ is a function of $\theta_i$ and latitude: as $\theta_i$ increases, $\rho_d$, and therefore $d$, do as well. After $\rho_d$ is determined for a node, $d$ is calculated and used to find the slice corners.

The special cases in which there is no adjacent node on one side or the other are handled by finding two of the four slice corners in the usual method and then reflecting the corners across the axis perpendicular to the line joining the two nodes.

This method for calculating the shapes for each slice is incorporated into the ASCAT SZF SIR code, using modified SIR code from ERS as a basis. With these modifications, the ASCAT SIR code reads in all node measurements for a given region of interest (i.e., for given lat/lon coordinates and date range), calculates the slice shape for each measurement, and then performs the SIR algorithm.

We note that although there are several approximations involved in this process, the SIR images are relatively insensitive to reasonable changes in these values. Changing values such as the antenna beamwidth or mean altitude of the platform affect the final image only slightly. However, the data reported from the near or far ends of the antenna swath occasionally produce artifacts in the SIR output. These data have high or low values of incidence angle, $\theta_i$.

The SZR data contain incidence angles approximately in the range from 34° to 60°. The incidence angle range of the SZF data is wider, so we match the range from the SZR data and discard measurements outside that range. The incidence angle range of the middle two beams is further trimmed to 55° to reduce artifacts. In the end, only $\sigma^0$ measurements such that

$$\theta_i \in \begin{cases} 34^\circ - 55^\circ & \text{for the two middle beams} \\ 34^\circ - 60^\circ & \text{for the four outer beams} \end{cases} \tag{2}$$

are retained for SZF data.

## 3. TUNING SIR PARAMETERS

The SIR algorithm has four parameters that are tuned for each instrument it is applied to. First is the number of iterations ($N_{\text{its}}$) of SIR. Iterating more than necessary is a waste of computation and amplifies noise, so the optimal value is one that allows the SIR algorithm to converge with few iterations. The next two parameters are the $\mathcal{A}$ and $\mathcal{B}$ initialization values ($A_{\text{init}}$ and $B_{\text{init}}$). Each pixel in the $\mathcal{A}$ and $\mathcal{B}$ images starts at the initialization value and is updated with each iteration of SIR. We choose values so the number of iterations needed is reduced. The final parameter is the $\mathcal{B}$-value weighting. The weighting accelerates convergence; however, too much weighting amplifies noise.

### 3.1. Determining optimum parameter values

To find optimum SIR parameter values, we start with default values from ERS and follow a procedure based on previous work with tuning SIR parameters [4, 5]: using a series of truth images, Monte Carlo simulated measurements are synthetically created from the true image using the geometry of an actual pass. SIR is performed on the simulated measurements for a variety of different SIR parameter values. Using various metrics, we compare SIR outputs with the truth images and choose SIR parameter values that lead to the overall best metric values. Finding optimum SIR parameters for the known truth images generally leads to good results using the actual ASCAT data.

To create the simulated measurements using the truth images, we require another parameter: $K_p$, the radiometric resolution, or radiometric accuracy. It is a measure of the noisiness of the data. $K_p$ is reported for SZR data but is not reported for SZF data. We assume a worst-case scenario and use a constant estimated value of $K_p$ for the simulated measurements.

The first SIR parameters to be determined are $N_{\text{its}}$, the number of iterations, and $B_{\text{weight}}$, the $\mathcal{B}$-weighting factor. We run the SIR algorithm on the simulated measurements with different values for

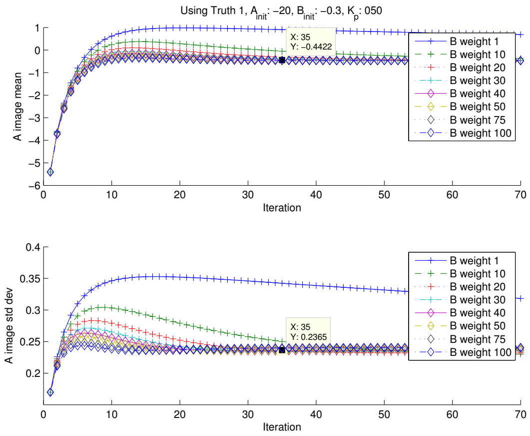

**Fig. 2**. A sample tuning plot. Various $\mathcal{B}$-weighting values are shown, with $N_{\text{its}}$ on the horizontal axis. For a particular choice $A_{\text{init}}$, $B_{\text{init}}$, and $K_p$, we compare this with other plots using the mean value and standard deviation of the SIR image to select optimum parameter values.

**Table 1**. Final ASCAT SIR parameters

| | |
|---|---|
| Number of iterations | SZR $N_{\text{its}} = 27$, SZF $N_{\text{its}} = 35$ |
| $\mathcal{A}$ initialization | $A_{\text{init}} = -15$ |
| $\mathcal{B}$ initialization | $B_{\text{init}} = -0.25$ |
| $\mathcal{B}$ weighting factor | $B_{\text{weight}} = 50$ |

$A_{\text{init}}$, $B_{\text{init}}$, and $K_p$. Constant-value truth images are used in this case. After each SIR iteration, we take the difference between the truth image and the SIR output and calculate the mean and standard deviation for both $\mathcal{A}$ and $\mathcal{B}$ values. A sample plot showing various $B_{\text{weight}}$ and $N_{\text{its}}$ values for a particular set of $A_{\text{init}}$, $B_{\text{init}}$ and $K_p$ is shown in Fig. 2. From a comparison of these plots, $N_{\text{its}} = 35$ provides sufficient iterations to converge in mean for both $\mathcal{A}$ and $\mathcal{B}$ for SZF data. For SZR data, the value formerly used for ERS, $N_{\text{its}} = 27$, is suitable for convergence in the mean.

Higher values of $B_{\text{weight}}$ cause $\mathcal{A}$ and $\mathcal{B}$ to converge more quickly. Without any noise ($K_p = 0$), the results suggest that $B_{\text{weight}}$ could be arbitrarily high. However, with noise, higher $B_{\text{weight}}$ amplifies the noise and increases the standard deviation in the SIR output. The value used for ERS, $B_{\text{weight}} = 50$, is kept for ASCAT for both SZR and SZF data, since the simulation results show that it is a good compromise between values that are too low—increasing the iterations to convergence—or too high—unduly adding noise.

Different values for $A_{\text{init}}$ and $B_{\text{init}}$ are tested using a different truth image: it consists of a homogeneous background with a radial gradient and darker lines to simulate rivers and other land features [5]. We use four metrics to analyze the resulting $\mathcal{A}$ and $\mathcal{B}$ images: mean error, standard deviation, RMS error, and the correlation coefficient. We conclude that the $\mathcal{A}$ and $\mathcal{B}$ initialization values should be set below the mean $\mathcal{A}$ and $\mathcal{B}$ values on the order of 0.5 dB and 0.05 dB/°, respectively. Using the $\mathcal{A}$ and $\mathcal{B}$ means from actual ASCAT data, we conclude that the final initialization values should be $A_{\text{init}} = -15$ and $B_{\text{init}} = -0.25$. The final SIR parameter values are listed in Tab. 1.

### 3.2. AVE images and grid sizing

The initial iteration of SIR is termed AVE: each pixel on a high resolution grid represents the average of the $\sigma^0$ measurements covering that pixel weighted by the measurement's spatial response function. Both $\mathcal{A}$ and $\mathcal{B}$ images are produced with AVE. In order for SIR/AVE to estimate $\mathcal{B}$ for a location, the measurements in the region must have adequate diversity in incidence angle, $\theta_i$. However, some 24-hour regions do not have dense enough sampling to estimate $\mathcal{B}$ at some locations. We thus update the AVE processing method to accommodate this.

We first compute the $\mathcal{A}$ and $\mathcal{B}$ AVE images but flag pixels with a standard deviation in incidence angle $\theta_i$ below a threshold. Often, these flagged pixels are in regions of the image where there is an accurate $\mathcal{B}$ estimate from a previous date range. We use precomputed AVE outputs for different date ranges as inputs and substitute the $\mathcal{B}$ pixels for all the flagged pixels in the current date range. If a flagged pixel cannot be replaced with a prior value, then a mean value is used instead. Finally, a 3x3 median filter is performed on the $\mathcal{B}$ AVE to smooth extreme values and the $\mathcal{A}$ AVE is recomputed using the improved $\mathcal{B}$ AVE.

With corrected AVE images, the AVE can seed the SIR iterations, removing the necessity of using $A_{\text{init}}$ and $B_{\text{init}}$ values. The SIR implementation for QuikSCAT similarly uses AVE to initialize SIR. A comparison of SIR outputs using AVE seeding versus constant initialization values shows some small differences in the regions where the flagged pixels were. These differences are expected. Noting the QuikSCAT SIR processing also uses AVE to initialize SIR processing and to maintain consistency, we use AVE to initialize the SIR algorithm for ASCAT.

To be compatible with prior scatterometer images, there are three choices for pixel resolution: 8.9 km/pixel, 4.45 km/pixel, or 2.225 km/pixel. Choosing a higher resolution potentially results in finer image detail, but quantization errors are aggravated, leading to more empty pixels in the image. To determine the optimal pixel resolutions, we compare SIR images made using the three available resolutions. We subjectively find the best results to be a pixel resolution of 8.9 km/pixel for SZR data and 4.45 km/pixel for SZF data.

Figure 3 shows zoomed portions of $\mathcal{A}$ SIR images processed using ASCAT data for a 24-hour period in Antarctica, and for a four-day period in North America. From these comparisons, we see that resolution enhancement has definitely been achieved. The SZF data yield higher resolution images than SZR data.

## 4. PRELIMINARY ASCAT SIR ANALYSIS

In this paper, we assume that the $\sigma^0$ value for a surface is the same regardless of the azimuth direction from ASCAT. This assumption is valid for many areas of interest on the Earth, but it does not hold over some regions, particularly eastern Antarctica. This is an effect documented previously for ERS and QuikSCAT [7, 8]. Accounting for the variations in $\sigma^0$ according to azimuth angle is referred to as azimuth modulation and has been performed for some previous scatterometers. We have yet to apply this to ASCAT but will do so in subsequent work.

A comparison of ASCAT slice images with QuikSCAT slice images show that the effective resolution for ASCAT slice images is lower than that of QuikSCAT. Because the slice sizes for ASCAT and QuikSCAT are comparable in size, we speculate that the ASCAT nodes are smoothed in the range direction, lengthening the size of the true $\sigma^0$ spatial extent beyond what we assume in this paper.

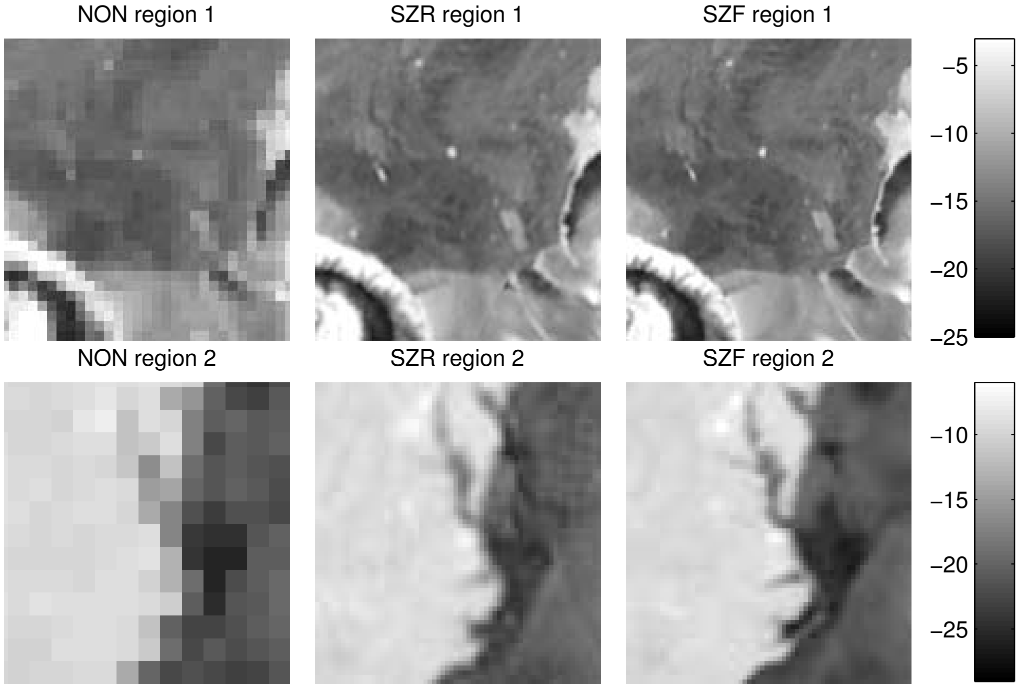

**Fig. 3**. The top row is a comparison of a region of Antarctica (JD 214 2008) and the bottom row similarly shows a section of the coast of North Carolina (JD 257–260 2009). The first column is the $\mathcal{A}$ NON (non-enhanced resolution at a pixel resolution of 17.8 km/pixel) image using SZF data. The second and third columns are $\mathcal{A}$ SIR images using SZR (8.9 km/pixel) and SZF data (4.45 km/pixel), respectively.

Wider effective slice widths would account for the lower effective resolution of ASCAT compared to QuikSCAT.

In comparing SIR images for ASCAT and QuikSCAT, we additionally note that the variance in $\sigma^0$ error over ocean is greater for QuikSCAT than for ASCAT. Also, $\sigma^0$ error variance over land is greater for ASCAT than for QuikSCAT. This difference can be exploited to aid in sea ice detection and estimation.

## 5. CONCLUSION

This paper has detailed the implementation of the SIR algorithm with ASCAT data. Implementing SZR data required few changes to extant ERS SIR code, whereas implementing SZF data required an estimation of the spatial extent for each node measurement. We have settled upon the overall best SIR parameter values. A visual comparison of the images reveals (not surprisingly) that SZF data is at a finer resolution than SZR data.

The ASCAT SIR images can be used for many scientific studies. ASCAT SIR data is already being operationally used at NOAA (National Oceanic and Atmospheric Administration) for monitoring ice and the recent Deepwater Horizon oil leak. With the availability of ASCAT SIR data, we extend the time-series of C-band scatterometer data previously updated with the ERS scatterometers. ASCAT C-band SIR data is also useful in comparisons with Ku-band QuikSCAT SIR data.

## 6. REFERENCES

[1] J. Figa-Saldaña, J. J. W. Wilson, E. Attema, R. Gelsthorpe, M. R. Drinkwater, and A. Stoffelen, “The advanced scatterometer (ASCAT) on the meteorological operational (MetOp) platform: A follow on for European wind scatterometers,” *Canadian Journal of Remote Sensing*, vol. 28, no. 3, pp. 404–412, 2002.

[2] D. S. Early and D. G. Long, “Image Reconstruction and Enhanced Resolution Imaging from Irregular Samples,” *IEEE Transactions on Geoscience and Remote Sensing*, vol. 39, no. 2, pp. 291–302, 2001.

[3] D. G. Long, P. Hardin, and P. Whiting, “Resolution Enhancement of Spaceborne Scatterometer Data,” *IEEE Transactions on Geoscience and Remote Sensing*, vol. 31, pp. 700–715, 1993.

[4] Q. P. Remund, “Refinement of SIRF for SASS,” Tech. Rep., BYU MERS Technical Report #98-04, 1998.

[5] Q. P. Remund and D. G. Long, “Optimization of SIRF for NSCAT,” Tech. Rep., BYU MERS Technical Report #97-03, 1997.

[6] I. S. Ashcraft and D. G. Long, “The spatial response function of SeaWinds backscatter measurements,” in *Proceedings of SPIE: Earth Observing Systems VIII*, W.L. Barnes, Ed., 3-6 Aug. 2003, vol. 5151.

[7] D. S. Early and D. G. Long, “Azimuth Modulation of C-band Scatterometer Sigma-0 Over Southern Ocean Sea Ice,” *IEEE Transactions on Geoscience and Remote Sensing*, vol. 35, no. 5, pp. 1201–1209, 1997.

[8] Q. P. Remund, D. S. Early, and D. G. Long, “Azimuth Modulation of Ku-band Scatterometer Sigma-0 over the Antarctic,” Tech. Rep., BYU MERS Technical Report #97-02, 1997.